



Multi-scale crystal plasticity finite element model approach to modeling nickel-based superalloys

Shahriyar Keshavarz, Somnath Ghosh *

Department of Civil Engineering, Johns Hopkins University, Baltimore, MD 21218, USA

Received 5 April 2013; received in revised form 8 July 2013; accepted 22 July 2013

Available online 15 August 2013

Abstract

This paper develops a homogenized, activation energy-based crystal plasticity (AE-CP) model for single-crystal Ni-based superalloys that can be implemented in simulations of polycrystalline aggregates. A size-dependent, dislocation-density-based finite element model of the subgrain scale representative volume element with explicit depiction of the γ - γ' morphology is developed as a building block for homogenization. Consistent with observations made in the temperature range $650\text{ }^\circ\text{C} \leq \theta \leq 800\text{ }^\circ\text{C}$, mechanisms of subgrain-scale anti-phase boundary shearing and grain-scale microtwinning are included in the model. The homogenized AE-CP model develops functional forms of constitutive parameters in terms of characteristics of the subgrain γ - γ' microstructural morphology. Specifically, the thermal shear resistance, reference plastic shear strain rate and saturation shear resistance are expressed as functions of γ' shape, volume fraction and γ channel width in the subgrain microstructure. This homogenized model has the advantage of significantly expediting crystal plasticity finite element simulations due to parameterized representation of the morphology, while retaining accuracy with respect to the explicit representation. A microtwin nucleation and evolution model is introduced in the grain-scale crystal plasticity framework for predicting tension–compression asymmetry. The model is validated with results of single-crystal tension and compression tests available in the literature.

© 2013 Acta Materialia Inc. Published by Elsevier Ltd. All rights reserved.

Keywords: Ni-based superalloys; Homogenization; Crystal plasticity; Morphology; Microtwin

1. Introduction

Ni-based superalloys are widely used in the aerospace industry, especially in hot sections of turbine engine components, such as blades, disks, casings and liners [1]. Their superior properties, including their strength, toughness, oxidation and creep resistance, and high-temperature stability, are attributed to the underlying subgrain γ - γ' microstructure [2], as shown in Fig. 1. The continuous γ -matrix phase is predominantly an alloy of Ni, Cr and other alloying elements, and has a face-centered cubic (fcc) lattice structure. The precipitate phase γ' is a coherent, ordered Ni₃Al inter-metallic of $L1_2$ crystal structure, which often appears as a distribution of precipitates. Their shape and

size depend largely on the cooling rate [3,4], as well as on the internal stress-gradients [5] encountered during casting and heat-treatment processes. The precipitates act as obstacles to the motion of dislocations, which either loop around or shear the precipitates, depending on the temperature and stress level. The volume fraction of γ' precipitates, their mean size and spacing have a major effect on the mechanical properties of these superalloys [6,7].

The deformation behavior under various loading and temperature conditions has been studied extensively, both for single-crystal [8,9] and polycrystalline [10,11] Ni-based superalloys. At lower temperatures ($\theta < 650\text{ }^\circ\text{C}$) and moderate stresses ($\sim 650\text{ MPa}$), creep mechanism is governed by dislocation-based shearing processes, whereas at higher temperatures ($\theta > 800\text{ }^\circ\text{C}$), creep deformation is controlled by Orowan looping and cross-slip mechanisms [7]. In the intermediate range of temperatures ($650\text{ }^\circ\text{C} \leq \theta \leq 800\text{ }^\circ\text{C}$)

* Corresponding author. Tel.: +1 410 516 7833; fax: +1 410 516 7473.

E-mail address: sghosh20@jhu.edu (S. Ghosh).

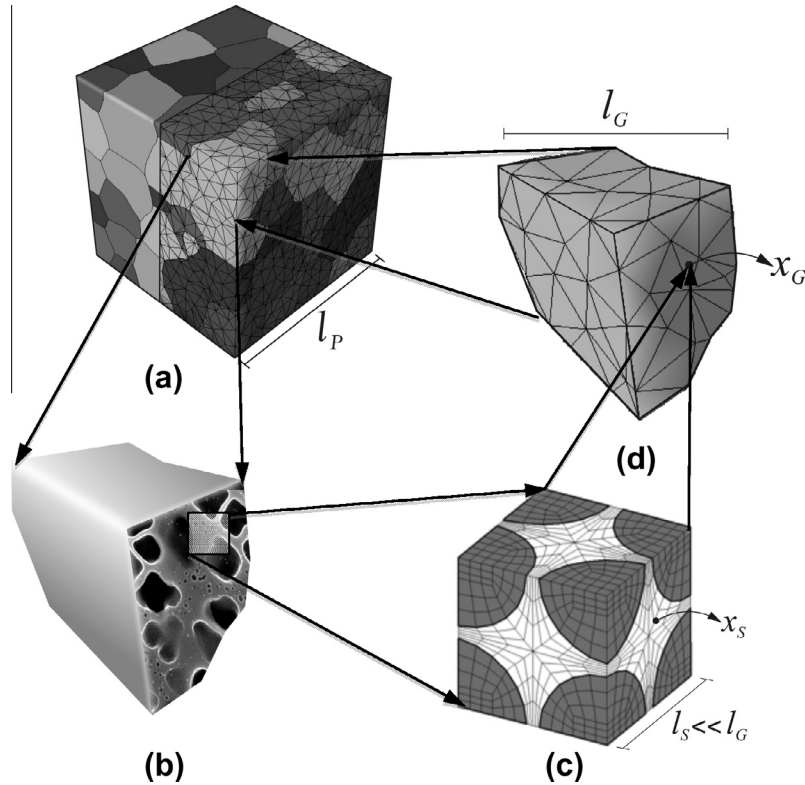


Fig. 1. Schematic representation of multiple scales in the development of a crystal plasticity finite element model for Ni-based superalloys: (a) polycrystalline microstructure showing the CPFEM mesh, (b) subgrain γ - γ' microstructure in a single grain, (c) discretized subgrain γ - γ' microstructural RVE and (d) homogenized crystal plasticity FE model for a grain.

and moderate stress levels (~ 650 MPa), dominant deformation mechanisms include anti-phase boundary (APB) shearing and microtwinning. This is the temperature-stress range considered in this paper. The probability of occurrence of each mechanism depends on the load and microstructural parameters, e.g. crystal orientation and morphology.

Modeling polycrystalline behavior of Ni-based superalloys is governed by features on three dominant scales: (i) the subgrain scale, characterized by the size of γ' precipitates and their spacing or γ channel width; (ii) the grain scale of single crystals, characterized by grain-boundary distance; and (iii) the scale corresponding to representative volume elements of polycrystalline aggregates. Crystal plasticity models should hierarchically incorporate information at each scale for generating constitutive models that can be implemented for microstructure–property relations, as well as microstructure design. Mesoscale analyses of superalloys, incorporating precipitate distributions as well as grain structure, have been conducted using phenomenological viscoplastic constitutive laws in Refs. [12–16]. Hardening parameters in many of the constitutive models have been expressed as assumed functions of the average precipitate size. Crystal plasticity finite element models (CPFEM) have been developed to model size-dependent creep and deformation response of single-crystal and polycrystalline Ni-based superalloys, e.g. in Refs. [17,18]. Analytical mod-

els have been proposed using simplifying assumptions for dislocation distributions under uniaxial and monotonic loads in Ref. [19]. Computational models of fatigue life prediction have used linear elastic fracture mechanics without explicit microstructural representation in Ref. [20]. Crystal plasticity models with implicit dependencies on the grain size, and precipitate size and volume fraction have been postulated for random distribution of precipitates in Ref. [21]. Dislocation-density-based hierarchical crystal plasticity models of creep and fatigue have been proposed in Refs. [22–26], where the dependence of mechanical properties on microstructural characteristics such as average γ' precipitate size and volume fraction are accommodated by parameters obtained by fitting with experimental data. The artificial neural network algorithm is used in these studies to develop rate-dependent macroscopic internal state variable constitutive models that implicitly account for grain size, precipitate volume fraction and size distribution. These experimental and computational studies on Ni-based superalloys illustrate the need for incorporating critical microstructural features in plasticity models for understanding the role of microstructure on mechanical behavior.

It is computationally intractable to model polycrystalline microstructures of superalloys using CPFEM, with explicit representations of the subgrain γ - γ' microstructure. Methods of nonlinear homogenization models, e.g. those

based on the asymptotic expansion theory [27,28], may be used to overcome this shortcoming. Most of these homogenization models solve the micromechanical representative volume element (RVE) problem at each element integration point in the computational domain to set up incremental stiffnesses in the macroscopic domain. This process can, however, lead to prohibitively large computational costs for CPFEM simulations of polycrystalline aggregates. To avert this limitation, Ghosh et al. have used the homogenization theory to develop constitutive models that incorporate parametric forms of microstructural variables and their evolution, for problems of polycrystalline plasticity [29], damage in composites [30] and ductile fracture of heterogeneous metals [31]. The parametric forms and their evolution can accurately represent the effect of microstructural morphology and deformation mechanisms. The methods yield a significant efficiency advantage, since the microstructural RVE problem need not be solved anymore.

This paper is aimed at developing a homogenized grain-scale crystal plasticity model with parametric representations of the subgrain morphology in its evolution laws. A schematic view of the multiscale problem, ranging from the heterogeneous subgrain γ - γ' microstructure to the mesoscale polycrystalline ensemble, is shown in Fig. 1. A sequence of steps is pursued to systematically create a hierarchical framework for realizing this model. The first step involves the development of a crystal plasticity finite element or CPFEM model of a subgrain scale representative volume element or RVE, delineating the explicit γ - γ' morphology. The CPFEM model incorporates a size-dependent dislocation-density-based crystal plasticity model [32,33], in which signed dislocation densities are explicit variables. The mechanism of APB shearing of γ' precipitates by matrix dislocations is also introduced. The next step involves the development of an activation-energy-based crystal plasticity (AE-CP) model at the scale of single crystals from homogenization of the dislocation-density-based subgrain model. The homogenized model incorporates the effect of the discrete subgrain morphology through critical morphological parameters in the hardening evolution laws that reflect the effect of dislocation density distributions in the subgrain model. The resulting hierarchical model has the potential of significantly expediting CPFEM simulations, while retaining accuracy.

Section 2 of this paper introduces the subgrain scale dislocation density crystal plasticity constitutive laws with APB shearing of γ' precipitates. Section 3 provides a framework for an AE-CP model at the scale of single crystals. The procedure for homogenization to yield morphology-dependent constitutive parameters, their calibration and validation with subgrain RVE (SG-RVE) models as well as experimental results are discussed in Section 4. Section 5 briefly introduces nucleation and evolution models for microtwins in the grain-scale crystal plasticity model and probes its effect on tension-compression asymmetry in the creep response of single-crystal Ni-based superalloys.

The paper concludes this development with a summary in Section 6.

2. Subgrain scale model for the γ - γ' microstructural RVE

The material studied is a two-phase, binary Ni-based superalloy consisting of γ (pure Ni) and γ' (Ni₃Al) phases. At the temperature range considered in this study, $650\text{ }^\circ\text{C} \leq \theta \leq 800\text{ }^\circ\text{C}$, plastic deformation is accommodated through crystallographic slip on discrete slip systems, as well as by APB shearing of the γ' phase. These contribute to plastic anisotropy of the subgrain microstructure consisting of γ - γ' phases. A dislocation-density-based crystal plasticity model, proposed in Refs. [32,33], is implemented to model the rate-dependent plastic behavior. It incorporates evolution of statistically stored dislocations (SSDs) in the γ -channel due to various dislocation generation and annihilation mechanisms and geometrically necessary dislocations (GNDs) due to plastic strain gradients at geometrically incompatible locations, such as the matrix-precipitate interface and grain boundaries.

The constitutive model admits a multiplicative decomposition of the deformation gradient \mathbf{F} into an incompressible, inelastic component \mathbf{F}^p associated with pure slip, and an elastic component \mathbf{F}^e that accounts for elastic stretching and rigid-body rotations expressed as:

$$\mathbf{F} = \mathbf{F}^e \mathbf{F}^p, \quad \text{s.t. } \det \mathbf{F}^e > 1 \quad \text{and} \quad \det \mathbf{F}^p = 1 \quad (1)$$

The evolution of plastic deformation is expressed in terms of the plastic velocity gradient \mathbf{L}^p , the plastic shear rate $\dot{\gamma}^\alpha$ on the slip system α and the Schmid tensor $\mathbf{s}_0^\alpha \equiv \mathbf{m}_0^\alpha \otimes \mathbf{n}_0^\alpha$ (in terms of the slip direction \mathbf{m}_0^α and slip plane normal \mathbf{n}_0^α in the reference configuration) as:

$$\mathbf{L}^p = \dot{\mathbf{F}}^p \mathbf{F}^{-p} = \sum_{\alpha=1}^N \dot{\gamma}^\alpha \mathbf{m}_0^\alpha \otimes \mathbf{n}_0^\alpha = \sum_{\alpha=1}^N \dot{\gamma}^\alpha \mathbf{s}_0^\alpha \quad (2)$$

The stress-strain relation invokes the second Piola-Kirchhoff stress \mathbf{S} and its work conjugate the Lagrange-Green strain tensor \mathbf{E}^e in the intermediate configuration as:

$$\mathbf{S} = \det(\mathbf{F}^e) \mathbf{F}^{e-1} \boldsymbol{\sigma} \mathbf{F}^{e-T} = \mathbf{C} : \mathbf{E}^e \quad \text{and} \quad \mathbf{E}^e \equiv \frac{1}{2} \{ \mathbf{F}^{eT} \mathbf{F}^e - \mathbf{I} \} \quad (3)$$

Here, \mathbf{I} is the identity tensor, \mathbf{C} is a fourth-order anisotropic elasticity tensor and $\boldsymbol{\sigma}$ is the Cauchy stress tensor. The plastic shearing rate on a slip system α is expressed by the Orowan equation as $\dot{\gamma}^\alpha = \rho_m^\alpha b v^\alpha$, where ρ_m^α is the density of mobile dislocations, b is the Burgers vector and v^α is the velocity of dislocations on the slip system α . The velocity of dislocations is a function of the applied shear stress τ^α , the slip system passing stress τ_{pass}^α and other slip system resistances, and is written as [32,33]:

$$v^\alpha = \lambda v \exp \left\{ -\frac{Q}{k_B \theta} \left(1 - \frac{|\tau^\alpha| - \tau_{pass}^\alpha}{\tau_{cut}^\alpha} \right) \right\} \text{sgn}(\tau^\alpha) \quad (4)$$

where λ is the distance moved by the dislocation depending on the probability of overcoming barriers, v is the oscillation frequency, Q is the activation energy, k_B is the Boltzmann's constant and θ is the absolute temperature. The slip system resistances are represented in terms of the passing stress τ_{pass}^α and the cutting stress τ_{cut}^α , and $\langle \bullet \rangle$ is the Macaulay bracket. The passing stress τ_{pass}^α occurs due to the interaction of mobile dislocations with other dislocations and their networks in the slip plane. The back stress is incorporated in the passing stress, which has an initial threshold value until the start of plastic shear strain in each slip system. The cutting stress τ_{cut}^α is due to the mobile dislocations cutting the forest dislocations with density ρ_F^α , perpendicular to the slip plane. These are expressed as:

$$\tau_{pass}^\alpha = c_1 G b \sqrt{\rho_P^\alpha + \rho_m^\alpha} \quad \text{and} \quad \tau_{cut}^\alpha = \frac{Q \sqrt{\rho_F^\alpha}}{c_2 b^2} \quad (5)$$

where c_1 and c_2 are material constants and G is the shear modulus. Contributions to the overall slip resistance are assumed to be due to both the density of immobile, statistically stored dislocations ρ_{SSD}^α and the vector field of GND density ρ_{GND}^α . The rate of evolution of ρ_{SSD}^α is the net effect of components due to lock formation, dipole formation, athermal annihilation and thermal annihilation [32,33], i.e.

$$\begin{aligned} \dot{\rho}_{SSD}^\alpha &= \dot{\rho}_{SSD_{lf}}^{\alpha+} + \dot{\rho}_{SSD_{df}}^{\alpha+} + \dot{\rho}_{SSD_{aa}}^{\alpha-} + \dot{\rho}_{SSD_{ta}}^{\alpha-} \quad \text{where} \\ \dot{\rho}_{SSD_{lf}}^\alpha &= \frac{c_3}{b} \sqrt{\rho_F^\alpha} \dot{\gamma}^\alpha, \\ \dot{\rho}_{SSD_{df}}^\alpha &= \frac{c_4}{b} \frac{\sqrt{3} G b}{16\pi(1-\nu)} (|\tau^\alpha| - \tau_{pass}^\alpha)^{-1} \rho_m^\alpha \dot{\gamma}^\alpha, \\ \dot{\rho}_{SSD_{aa}}^\alpha &= -c_5 \rho_{SSD}^\alpha \dot{\gamma}^\alpha \quad \text{and} \\ \dot{\rho}_{SSD_{ta}}^\alpha &= -c_6 \frac{D_0 b^3}{k_B \theta} \exp\left(\frac{-Q_{bulk}}{k_B \theta}\right) (\rho_{SSD}^\alpha)^2 |\tau^\alpha| \left(\frac{\dot{\gamma}^\alpha}{\dot{\gamma}_{ref}^\alpha}\right)^{c_7} \end{aligned} \quad (6)$$

Here, c_3 , c_4 , c_5 , c_6 and c_7 are material constants, D_0 is the diffusion coefficient, Q_{bulk} is the activation energy for dislocation climb and $\dot{\gamma}_{ref}^\alpha$ is a reference shear rate. Increments of the screw, edge and normal components of the GND density are derived from the material time derivative of the Nye's dislocation tensor $\dot{\mathbf{A}} = (\sum_{\alpha=1}^N \dot{\mathbf{A}}^\alpha)$ as:

$$\begin{aligned} \dot{\rho}_{GND_s}^\alpha &= \frac{1}{b} [\nabla_X \times (\dot{\gamma}^\alpha \mathbf{F}_P^T \mathbf{n}^\alpha)] \cdot \mathbf{m}^\alpha, \\ \dot{\rho}_{GND_{det}}^\alpha &= \frac{1}{b} [\nabla_X \times (\dot{\gamma}^\alpha \mathbf{F}_P^T \mathbf{n}^\alpha)] \cdot \mathbf{t}^\alpha, \\ \dot{\rho}_{GND_{den}}^\alpha &= \frac{1}{b} [\nabla_X \times (\dot{\gamma}^\alpha \mathbf{F}_P^T \mathbf{n}^\alpha)] \cdot \mathbf{n}^\alpha \end{aligned} \quad (7)$$

where \mathbf{m}^α , \mathbf{n}^α and $\mathbf{t}^\alpha = (\mathbf{n}^\alpha \times \mathbf{m}^\alpha)$ are unit vectors in the slip direction of the Burgers vector, normal to the slip plane α and tangent to the edge dislocation direction, respectively, and ∇_X is the gradient operator in the material coordinate system. The forest and parallel dislocation densities are written as functions of SSDs and GNDs, with an interaction strength coefficient $\chi^{\alpha\beta}$ between different slip systems [34], as:

$$\begin{aligned} \rho_F^\alpha &= \sum_{\beta=1}^N \chi^{\alpha\beta} [\rho_{SSD}^\beta |\cos(\mathbf{n}^\alpha, \mathbf{t}^\beta)| + \rho_{GND_s}^\beta |\cos(\mathbf{n}^\alpha, \mathbf{m}^\beta)| \\ &\quad + \rho_{GND_{det}}^\beta |\cos(\mathbf{n}^\alpha, \mathbf{t}^\beta)| + \rho_{GND_{den}}^\beta |\cos(\mathbf{n}^\alpha, \mathbf{n}^\beta)|] \\ \rho_P^\alpha &= \sum_{\beta=1}^N \chi^{\alpha\beta} [\rho_{SSD}^\beta |\sin(\mathbf{n}^\alpha, \mathbf{t}^\beta)| + \rho_{GND_s}^\beta |\sin(\mathbf{n}^\alpha, \mathbf{m}^\beta)| \\ &\quad + \rho_{GND_{det}}^\beta |\sin(\mathbf{n}^\alpha, \mathbf{t}^\beta)| + \rho_{GND_{den}}^\beta |\sin(\mathbf{n}^\alpha, \mathbf{n}^\beta)|] \end{aligned} \quad (8)$$

These evolve with SSDs and GNDs due to plastic deformation and hardening mechanisms. The density of mobile dislocations ρ_m^α is computed as a function of the forest and parallel dislocation density and temperature θ as [32]:

$$\rho_m^\alpha = \frac{2k_B \theta \sqrt{\rho_F^\alpha \rho_P^\alpha}}{c_1 c_2 G b^3} \quad (9)$$

2.1. Criteria for APB shearing in the γ' phase

Dislocations in the disordered fcc γ -phase do not initially enter the ordered γ' phase, characterized by crystal-line lattice $L1_2$. Transmission electron microscopy (TEM) studies [6] have shown that the matrix dislocations form super-dislocations at the γ - γ' interface and enter the γ' phase by APB shearing upon reaching a critical condition. In the present work, APB shearing of γ' phase is assumed to take place when the following conditions are met at the interface:

- (i) $\tau^\alpha > \tau_c$ (resolved shear stress on a slip system exceeds a critical value)
- (ii) $\rho_m^\alpha > \rho_c$ (mobile dislocation density exceeds a critical value)

(10)

The corresponding flow rule for the γ' phase is expressed as:

$$\begin{aligned} \dot{\gamma}^\alpha &= \mathbf{H}(\rho_m^\alpha - \rho_c) \rho_m^\alpha b \lambda v \\ &\quad \exp\left\{-\frac{Q}{K_B \theta} \left(1 - \frac{\langle \tau^\alpha - \tau_{pass}^\alpha \rangle \mathbf{H}(\tau^\alpha - \tau_c)}{\tau_{cut}^\alpha}\right)\right\} \text{sgn}(\tau^\alpha) \end{aligned} \quad (11)$$

where $\mathbf{H}(\bullet)$ is the Heaviside function, τ_c is the critical resolved shear stress and ρ_c is the critical density at the interface.

2.2. Calibration of parameters in the constitutive law

Selected parameters in the crystal plasticity model in Eqs. (1)–(11) are calibrated using single-crystal constant strain rate and tension creep experimental data for the alloy CMSX-4 in Refs. [35,36]. The alloy contains 70 vol.% of predominantly cuboidal γ' precipitates of average size 0.45 μm . The tensile constant strain rate test in Ref. [35] has been performed at a strain rate of 0.0001 s^{-1} at a temperature of 800 $^\circ\text{C}$. Creep tests in Ref. [36] have been done for a tensile load of 750 MPa at a temperature of 750 $^\circ\text{C}$. The average size of the RVE selected for these tests is 0.5 μm . For calibrating constitutive

parameters, constant strain rate and creep loading conditions are simulated by the CPFEM code for two-phase subgrain microstructures, as shown in Figs. 1c and 2a. Constants c_1 – c_7 in Eqs. (5) and (6) are calibrated from the experimental data in Ref. [35], while the critical shear stress τ_c and the threshold dislocation density ρ_c in Eq. (10) are calibrated from creep test results in Ref. [36]. Values of the calibrated parameters are listed in Table 1.

The elastic stiffness tensor $C_{\alpha\beta} = C_{\beta\alpha}$ ($\alpha = 1 \dots 6, \beta = 1 \dots 6$) is considered to be isotropic for both phases. For the γ phase, non-zero components of the stiffness tensor are [37]: $C_{11} = C_{22} = C_{33} = 201.7$ GPa, $C_{44} = C_{55} = -C_{66} = 104.5$ GPa, $C_{12} = C_{13} = C_{23} = 134.4$ GPa.

For the γ' phase, non-zero components of the stiffness tensor are: $C_{11} = C_{22} = C_{33} = 229.7$ GPa, $C_{44} = C_{55} = -C_{66} = 110.1$ GPa, $C_{12} = C_{13} = C_{23} = 153.2$ GPa. The shear modulus is expressed as: $G = \frac{1}{3}(C_{11} - C_{12} + C_{44})$.

The Burgers vector is $b = 2.49$ nm and the activation energy is $Q = 6.5 \times 10^{-19}$ J.

2.3. Validation of the subgrain CPFEM model

To validate the crystal plasticity constitutive relations with APB shearing, CPFEM simulation results are com-

pared with experimental data in Refs. [35,36]. The RVE is constructed for a regular array of cubic precipitates with a 70% precipitate volume fraction. Its dimensions are $0.5 \mu\text{m} \times 0.5 \mu\text{m} \times 0.5 \mu\text{m}$, with the edge length of cubic γ' particles allocated symmetrically at the eight corners in Fig. 2a is $0.45 \mu\text{m}$. Simulations are done for an applied strain rate of 0.0001 s^{-1} in the y -direction (slip system [010]) at a temperature of 800°C . The CPFEM model of the microstructural RVE is discretized using eight-noded trilinear brick elements using selective reduced integration. To emulate experimental conditions, a tensile constant strain rate is applied to the top y -surface, while rigid body modes are suppressed by applying boundary conditions on the bottom y -surface as $u_y = 0$ on all nodes, $u_x = 0$ on nodes on the line $x = 0.25 \mu\text{m}$ and $u_z = 0$ on nodes on the line $z = 0.25 \mu\text{m}$. An FE mesh convergence study is first conducted to examine mesh sensitivity to the results and decide on a converged mesh. Six different meshes, containing 216, 512, 1000, 1728, 2200 and 2744 brick elements, respectively, are considered and the volume-averaged stress in the y -direction and total GND density responses are compared. Error measures at a given strain are expressed as: (i) $e_\sigma = \frac{\bar{\sigma}_h - \bar{\sigma}_i}{\bar{\sigma}_h}$, where $\bar{\sigma}_h$ and $\bar{\sigma}_i$ are the volume-averaged stresses for a highly refined mesh containing 3375 elements

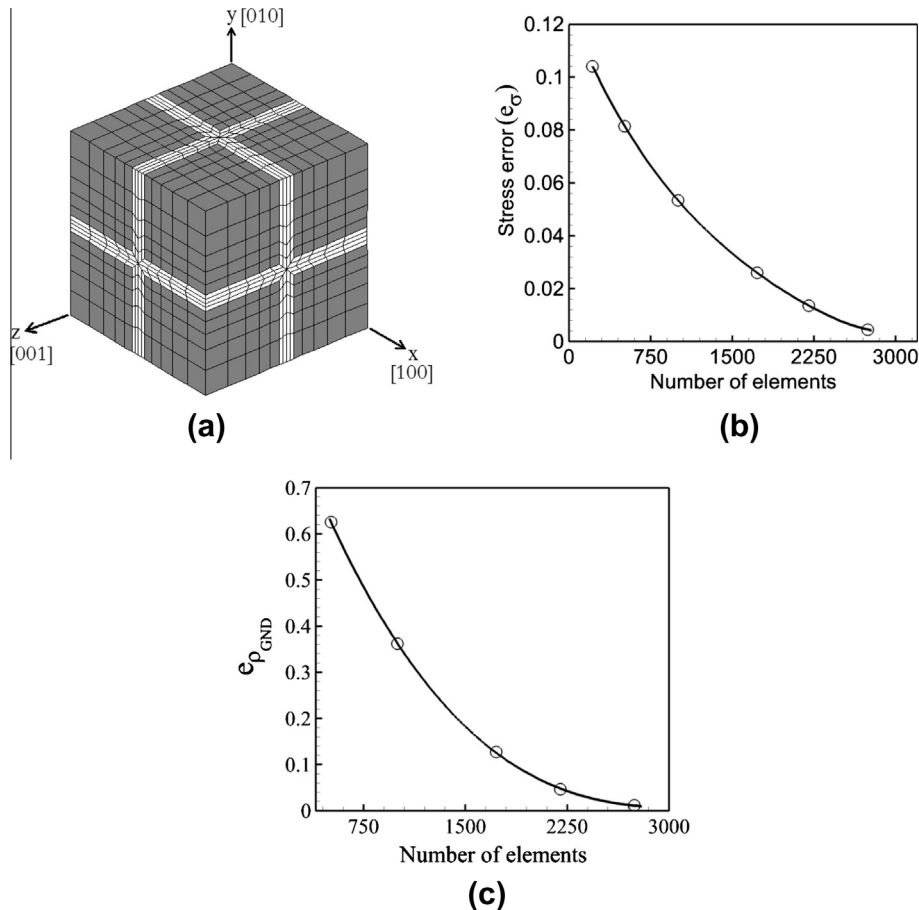


Fig. 2. CPFEM results for mesh convergence for a strain rate 0.0001 s^{-1} and 5% logarithmic strain: (a) FEM mesh for cubic precipitates with the volume fraction of 70% and edge length $0.5 \mu\text{m}$, (b) y -direction stress error e_σ as a function of mesh density and (c) GND dislocation density error $e_{\rho_{\text{GND}}}$ with mesh density.

Table 1
Calibrated parameters for the subgrain scale crystal plasticity model.

Constant	c_1	c_2	c_3	c_4	c_5	c_6	c_7	τ_c	ρ_c
Value	4.0	0.8	1.0×10^{-3}	1.0×10^{-4}	10.0	10.0	0.3	110 MPa	1.0×10^{11}

and each mesh, respectively; and (ii) $e_{\rho_{GND}} = \frac{(\rho_{GND})_h - (\rho_{GND})_i}{(\rho_{GND})_h}$, where $(\rho_{GND})_h$ and $(\rho_{GND})_i$ are the average GND density in the highly refined mesh and each mesh, respectively. These are plotted as a function of the number of elements in Fig. 2b and c. The error for 2200 elements with respect to the fine mesh is less than 5%, which demonstrates mesh convergence for the properties considered. From the convergence study, a FE mesh of 2200-elements for the RVE is considered to be accurate and is used for subsequent analyses. The volume-averaged stress–strain response is subsequently compared with experimental data in Fig. 3a. Good agreement is found between the experimental results and model predictions. The small difference may be attributed to the plastic response due to nonsymmetrical distribution of the γ' phase with varying γ channel width l_c , as well as their shapes. In the actual alloy, the channel width l_c and shapes can vary significantly from point to point in the material. The distribution of mobile dislocation density ρ_m along the x -axis is shown in Fig. 3b for three stages of deformation. In the initial stage, stage 1, both γ and γ' phases behave elastically and there is no plastic deformation in the domain. From stage 1 to stage 2, the γ phase experiences plastic deformation and SSDs start to evolve. With the evolution of SSDs, plastic strain gradient builds near the γ – γ' interfaces. Lattice continuity is preserved by the evolution of GNDs, which results in the evolution of mobile dislocation densities. There is very little difference in ρ_m for the first two stages in the γ' phase. However, this difference is significant in the γ -channel due to the evolution of GNDs. In the post-APB shearing stage, stage 3, the γ' phase experiences plastic deformation with a considerable rise in ρ_m .

3. Framework for the grain-scale crystal plasticity model

The proposed grain-scale, homogenized crystal plasticity model for fcc Ni-based superalloys with parameterized representation of the γ – γ' microstructure follows the framework of the AE-CP models proposed in Refs. [38–40]. The homogenized constitutive model incorporates an evolving thermal shear resistance as well as an athermal shear resistance due to plastic deformation. For a slip system α , the plastic shearing rate follows from the Orowan equation as:

$$\dot{\gamma}^\alpha = \begin{cases} 0 & \text{if } \tau_{eff}^\alpha \leq 0 \\ \dot{\gamma}_*^\alpha \exp \left\{ -\frac{Q}{k_B \theta} \left(1 - \left[\frac{|\tau_{eff}^\alpha|}{s_a^\alpha} \right]^p \right)^q \right\} \text{sgn}(\tau^\alpha) & \text{if } 0 \leq \tau_{eff}^\alpha \leq s_a^\alpha \end{cases} \quad (12)$$

Here Q is the activation energy barrier, $k_B (= 1.3807 \times 10^{-23} \text{ J K}^{-1})$ is the Boltzmann's constant, θ is the temperature, and the exponents p and q are material constants. For the slip system α , $\dot{\gamma}_*^\alpha$ is a reference strain rate and $\tau_{eff}^\alpha (= |\tau^\alpha| - s_a^\alpha)$ is the effective resolved shear stress. The temperature dependent critical slip resistance $s^\alpha (> 0)$ is assumed to comprise a thermally activated obstacle to slip s_a^α and a part due to the athermal obstacles s_*^α . The athermal and thermal shear resistances s_a^α and s_*^α correspond to the passing and cutting stress barriers, respectively. The difference between the athermal shear resistance and the resolved shear stress is the driving force for dislocation motion on the slip system α . Two specific issues arise with respect to variables in Eq. (12). The first concerns the reference strain rate $\dot{\gamma}_*^\alpha$, which is generally considered to be a constant for all slip systems. However, $\dot{\gamma}_*^\alpha$ can evolve with the activation of APB shearing, when the γ -phase

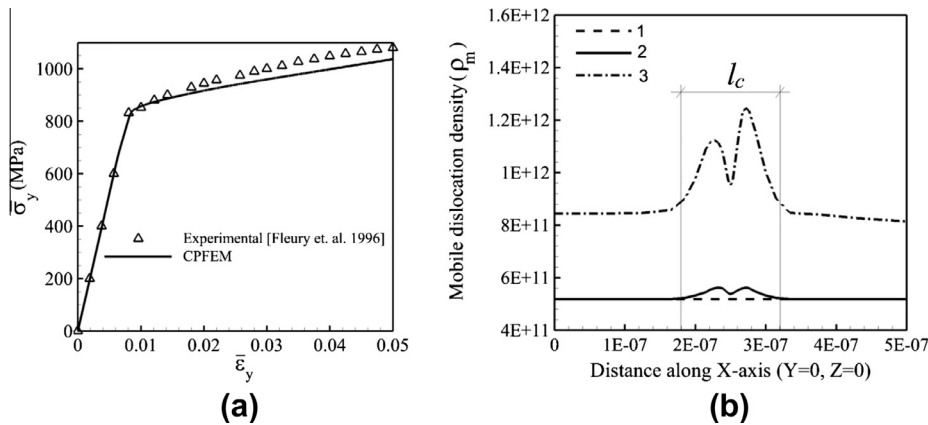


Fig. 3. CPFEM simulation results under an applied constant strain rate 0.0001 s^{-1} : (a) volume-averaged true stress–logarithmic strain response by CPFEM and tension experiment in Ref. [35], (b) distribution of mobile dislocation density along x -axis for three stages of deformation.

experiences plastic deformation with increasing dislocation density, especially near the γ – γ' interfaces. This deformation effect can be significant for some γ' precipitate shapes, e.g. spherical. To examine the effect of this on the reference strain rate $\dot{\gamma}_*$, a $0.25 \mu\text{m} \times 0.25 \mu\text{m} \times 0.25 \mu\text{m}$ RVE with spherical precipitates is simulated under a y -direction applied strain rate of 0.0001 s^{-1} at $800 \text{ }^\circ\text{C}$. The volume-averaged stress–strain response by the SG-RVE simulation is compared with the AE-CP model with constant $\dot{\gamma}_*$ in Fig. 4a. The difference near the initial yielding, corresponding to the initiation of APB shearing, is quite significant. This effect is, however, not as strong for cuboidal precipitates. The yield point phenomenon is captured by making the reference strain rate $\dot{\gamma}_*$ a function of plastic strain and morphological parameters [40] as:

$$\dot{\gamma}_* = H(\bar{\epsilon}_p - l_p) \dot{\gamma}_0 \left\{ \frac{\tanh(k) + \tanh(kl_p)}{10\{\tanh[k_*(\bar{\epsilon}_p - l_p)] + \tanh(kl_p)\}} - 1 \right\} + \dot{\gamma}_0 \quad (13)$$

where H is the Heaviside step function, $\dot{\gamma}_0$ corresponds to the initial strain rate and l_p, k, k_* are material constants. In this work, $l_p = 10^{-4}$ and k and k_* are derived in terms of morphological parameters in Section 4.4. The equivalent

plastic strain $\bar{\epsilon}_p (= \sqrt{\frac{2}{3} \epsilon_{ij}^p \epsilon_{ij}^p})$ is defined in terms of the Lagrangian plastic strain $\epsilon_{ij}^p = \frac{1}{2} (F_{ij}^{pT} F_{ij}^p - \delta_{ij})$. The corresponding stress–strain response, using the AE-CP constitutive model of Eqs. (12) and (13), is compared with the volume-averaged stress–strain response from the SG-RVE simulation in Fig. 4c. Significant improvement is observed with the introduction of the yield-point phenomenon by the functional form of the reference strain rate. Eq. (13) implicitly exhibits the influence of channel width (due to precipitate shape) on APB shearing nucleation. Plastic deformation in the channel starts at a stress of $\sim 600 \text{ MPa}$ both for spherical and cubic precipitates, as shown in Fig. 4. Significant evolution of SSDs and GNDs for spherical precipitates reduces the yield stress from around 850 MPa to 650 MPa , as shown in Fig. 4a. However, divergence from the subgrain model is observed at higher values of the equivalent plastic strain $\bar{\epsilon}_p$, where the response saturates. This is especially noticeable for cubic precipitates in Fig. 4b. In this plot, a constant value of the thermal slip resistance s_*^z is assumed [41]. This is the second issue in the activation-energy-based model that is not consistent with the subgrain level RVE model, which

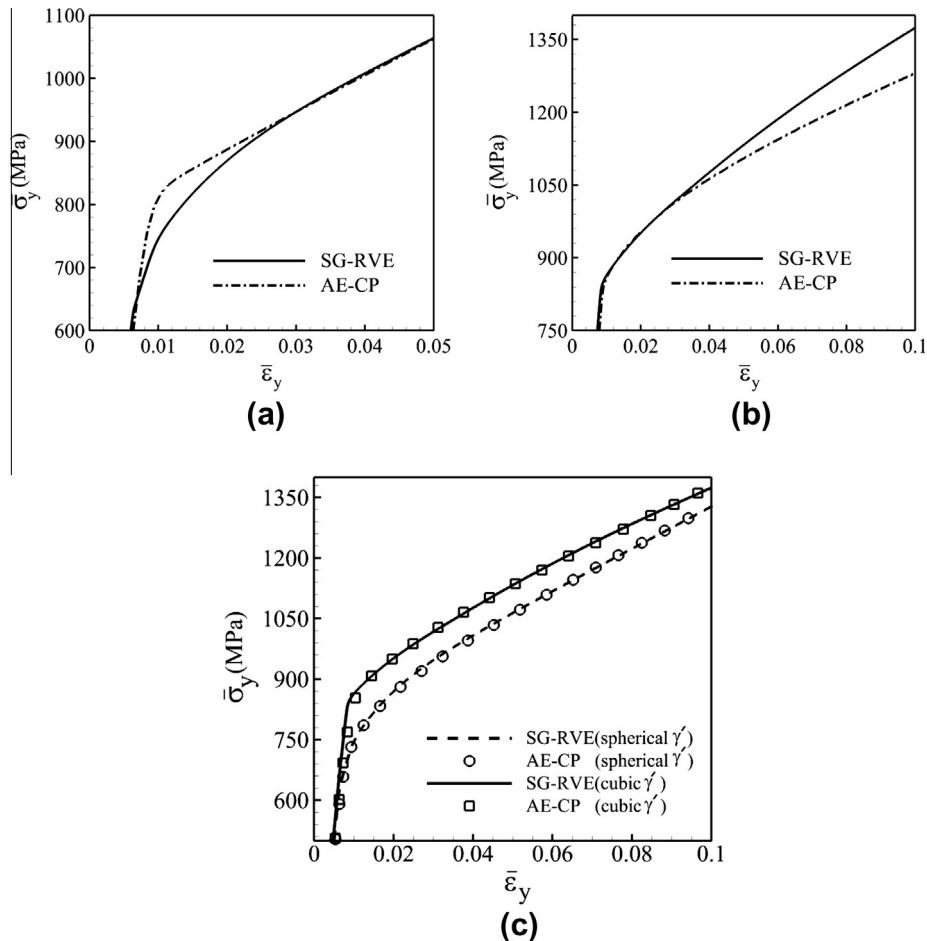


Fig. 4. Comparison of stress–strain response by the subgrain dislocation-density-based RVE model and the activation energy based crystal plasticity model: (a) with constant reference strain rate for spherical precipitates, (b) with evolving only athermal shear resistance for cubic precipitates, and (c) with variable reference strain rate and evolving thermal and athermal shear resistances.

accounts for forest dislocations in its hardening parameters in Eq. (5). Consequently, evolution laws for thermal and athermal shear resistances, contributing to the overall slip resistance s^α , are proposed in terms of the plastic strain rate. The thermal shear resistance accounting for forest dislocations normal to the slip plane and the athermal shear resistance reflecting the effect of parallel dislocations in the slip direction m^α are expressed as:

$$\dot{s}_a^\alpha = \sum_{\beta=1}^N h_a^{\alpha\beta} |\dot{\gamma}^\beta \sin(\mathbf{n}^\alpha, \mathbf{t}^\beta)|, \quad \dot{s}_*^\alpha = \sum_{\beta=1}^N h_*^{\alpha\beta} |\dot{\gamma}^\beta \cos(\mathbf{n}^\alpha, \mathbf{t}^\beta)| \quad (14)$$

where \mathbf{n}^α is slip-plane normal, $\mathbf{t}^\alpha = \mathbf{m}^\alpha \times \mathbf{n}^\alpha$, and the total shear resistance is $\dot{s}^\alpha = \sqrt{(\dot{s}_a^\alpha)^2 + (\dot{s}_*^\alpha)^2}$. For convenience, coefficients accounting for the interactions between slip systems are taken to be the same, i.e. $h_a^{\alpha\beta} = h_*^{\alpha\beta} = h^{\alpha\beta}$. Each component of $h^{\alpha\beta}$ is the deformation resistance on slip system α due to shearing on slip system β . It describes both self- and latent hardening as:

$$h^{\alpha\beta} = q^{\alpha\beta} h^\beta, \quad \text{where} \quad h^\beta = \left[h_0 \left(1 - \frac{s^\beta}{s_{sat}^\beta} \right)^r \right] \text{sign} \left(1 - \frac{s^\beta}{s_{sat}^\beta} \right) \quad (15)$$

The parameter h^β denotes the resistance-dependent self-hardening rate, s_{sat}^β is the saturation value of the reference shear stress and r is a constant exponent. The coefficient $q^{\alpha\beta} = q + (1 - q)\delta^{\alpha\beta}$, where q is a latent-hardening parameter chosen as 1.4. The stress–strain response by the AE-CP FE model with (i) variable reference strain rate $\dot{\gamma}_*$ and (ii) evolving thermal and athermal shear resistances $\dot{s}_a^\alpha, \dot{s}_*^\alpha$ is in excellent agreement with the SG-RVE model response in Fig. 4c for both cubic and spherical precipitates.

4. A homogenized AE-CP model from an SG-RVE model

The constitutive parameters in Eqs. (12)–(15) for the AE-CP model are assumed to be governed by the Hill–Mandel principle of macro–micro energy equivalence [42], where the micromechanical analysis is conducted with the SG-RVE model. The constitutive parameters are formulated in terms of critical morphological variables and are calibrated by computational homogenization of the SG-RVE model response.

4.1. Morphological parameters in the subgrain microstructural RVE

The subgrain microstructural RVE consists of γ' precipitates homogeneously distributed in a matrix phase γ , as shown in Fig. 1c. Three characteristic parameters representing the microstructural morphology are delineated as: (i) γ' volume fraction v_p ; (ii) γ' shape factor n ; and (iii) minimum channel width l_c between γ' precipitates. The volume fraction is expressed as the ratio of the γ' precipitate volume to the RVE volume, i.e. $v_p = \frac{V_{\gamma'}}{V_{RVE}}$. The shape factor is described in terms of the exponent of a generalized ellipsoid: $(\frac{x}{a})^n + (\frac{y}{b})^n + (\frac{z}{c})^n = 1$, where a, b , and c are the dimensions

of the three principal axes and n is the shape exponent. Here, $a = b = c$ is assumed to represent equiaxed precipitates. A value $n = 2$ corresponds to a sphere while $n \rightarrow \infty$ corresponds to a cube. To avoid a singular value of n , a transformed shape factor $n_1 = \tan^{-1}(n)$ is used in the parameterization.

The effect of these morphological parameters on the volume-averaged stress–strain response of the RVE using the subgrain dislocation density CPFÉ simulations is examined and depicted in Fig. 5. For each simulation conducted at 0.0001 s^{-1} and $800 \text{ }^\circ\text{C}$, one of the parameters is varied, while the other two are held constant. The variables considered are: (i) cubic precipitates of volume fractions 75.13% and 57.87%; (ii) shape factors $n = 2.0$ and ∞ ; and (iii) channel width $l_c = 0.29 \text{ } \mu\text{m}$ and $l_c = 0.58 \text{ } \mu\text{m}$ for cubic precipitates of 29.63% volume fraction. The results in Fig. 5 show that the post-yield plastic response does not change much with increasing volume fraction, even though the yield stress increases. The yield stress changes and the plastic response diverges with increasing strain for the different shapes. The plastic response changes with increasing channel width, while the yield stress decreases only slightly.

4.2. Morphology-dependent constitutive parameters in the CP model

Plastic slip and hardening parameters in the grain-scale AE-CP model are functions of the statistically stored and geometrically necessary dislocation densities. The SSDs do not generally change much with morphological variables, i.e. they are size independent, but the GNDs can vary significantly with precipitate shape and size. The forest and parallel dislocation densities are expressed as:

$$\begin{aligned} \rho_F(\rho_{SSD}, \rho_{GND}) &= \rho_F(\gamma^\alpha, \nabla\gamma^\alpha), \\ \rho_P(\rho_{SSD}, \rho_{GND}) &= \rho_P(\gamma^\alpha, \nabla\gamma^\alpha) \end{aligned} \quad (16)$$

Crystal plasticity hardening parameters are functions of the plastic slip γ^α due to SSDs. Morphological parameters should also be incorporated in these functions to account for the effect of GNDs or gradient of plastic shear strain $\nabla\gamma^\alpha$. Sensitivity analyses show that the initial thermal shear resistance and its rate, the reference slip-rate $\dot{\gamma}_*$ and the saturation shear stress s_{sat}^α are functions of the morphology. Thus, in Eqs. (13)–(15), the parameters $s_{*0}^\alpha(n_1, v_p, l_c)$, $\dot{s}_*^\alpha(n_1, v_p, l_c)$, $\dot{\gamma}_*(n_1, v_p, l_c)$ and $s_{sat}^\alpha(n_1, v_p, l_c)$ may be derived in terms of morphology as well as $(\gamma^\alpha, \nabla\gamma^\alpha)$ as:

$$\begin{aligned} \dot{s}_*^\alpha(n_1, v_p, l_c) &= \sum_{\beta=1}^N h^{\alpha\beta}(n_1, v_p, l_c) |\dot{\gamma}^\beta \cos(\mathbf{n}^\alpha, \mathbf{t}^\beta)| \\ &= \sum_{\beta=1}^N \left[h_0 \left(1 - \frac{s^\beta}{s_{sat}^\beta(n_1, v_p, l_c)} \right)^r \right] \text{sgn} \left(1 - \frac{s^\beta}{s_{sat}^\beta} \right) \\ &\quad |\dot{\gamma}^\beta \cos(\mathbf{n}^\alpha, \mathbf{t}^\beta)| \quad (\text{a}) \\ \dot{\gamma}_*(n_1, v_p, l_c) &= H(\bar{\epsilon}_p - l_p) \dot{\gamma}_0 \\ &\quad \left\{ \frac{\tanh[k(n_1, v_p, l_c)] + \tanh[k(n_1, v_p, l_c)l_p]}{10\{\tanh[k_*(n_1, v_p, l_c)(\bar{\epsilon}_p - l_p)] + \tanh[k(n_1, v_p, l_c)l_p]\}} - 1 \right\} \\ &\quad + \dot{\gamma}_0 \quad (\text{b}) \end{aligned} \quad (17)$$

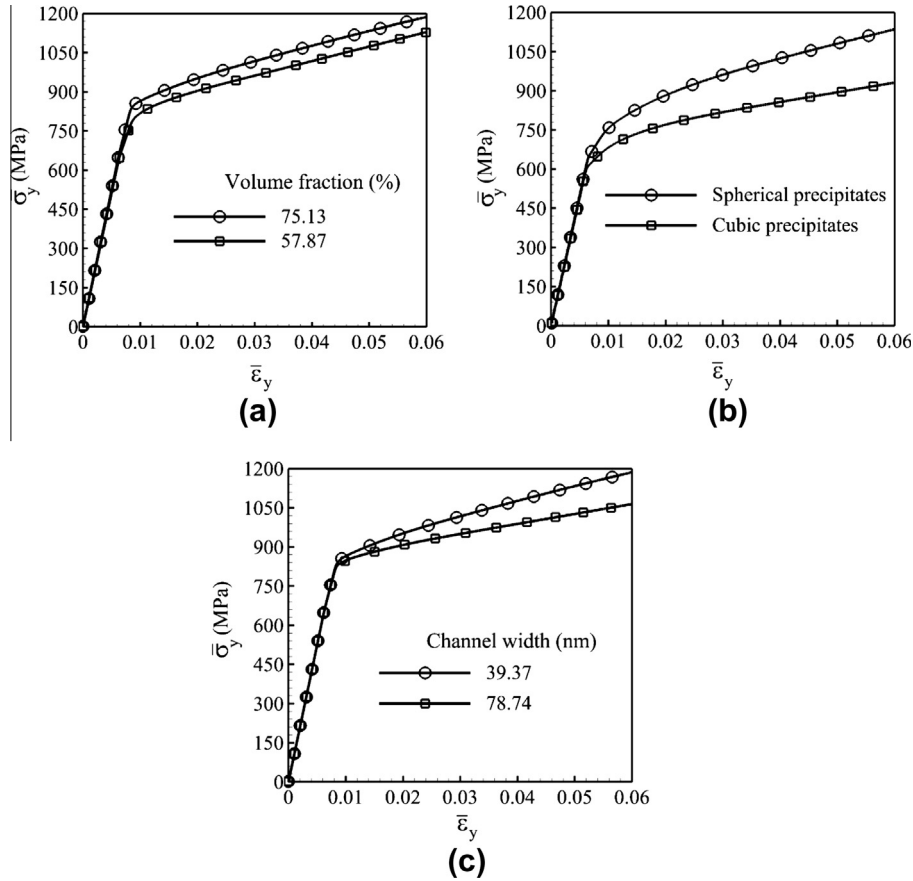


Fig. 5. Effect of γ' precipitate (a) volume fraction, (b) shape and (c) channel width for cubic precipitates with 29.63% volume fraction, on the stress–strain response under constant tensile strain rate of 0.0001 s⁻¹ at a temperature of 800 °C.

The initial strain rate $\dot{\gamma}_0$ and hardening parameter h_0 are insensitive to the morphology.

4.3. Calibrating the grain-scale crystal plasticity model parameters

Eqs. (12), (13), (14), (15), and (17) contain a number of material parameters, some of which vary with the morphology while others remain constant. The constant material parameters to be evaluated are the activation energy Q and exponents p , q in Eq. (12), $\dot{\gamma}_0$ in Eq. (13), and the hardening parameter h_0 and exponent r in Eq. (15). They are calibrated for the superalloy CMSX-4 single crystals using results of tension creep and constant strain rate experiments in Refs. [36] and [35], respectively. The tensile loading in the creep test is increased to 750 MPa and kept at this level for 100 h at 750 °C. The constant strain rate test is performed at a strain rate of 0.0001 s⁻¹. The γ – γ' morphological data in these tests, as implemented in the model, corresponds to a 70% volume fraction of cuboidal γ' precipitates of average size 0.45 μm in a 0.5 μm cubic RVE.

Calibrated values of the constant material parameters are listed in Table 2. Subsequently, the morphology-dependent parameters $s_{*0}^\alpha(n_1, v_p, l_c)$, $k_*(n_1, v_p, l_c)$, $k(n_1, v_p, l_c)$ and

$s_{sat}^\beta(n_1, v_p, l_c)$ in Eq. (17) are calibrated by comparing the stress–strain response from the AE-CP model in Eqs. (12)–(15), with the volume-averaged response from the SG-RVE model simulations for constant strain rate tests of 0.0001 s⁻¹ in the [0 10] direction at 800 °C. The calibration process involves 37 different RVE microstructures, viz.: (i) four microstructures with $n = 1.5$, $v_p = 0.2766$ and four different l_c 's; (ii) 16 microstructures with $n = 2.0$, $v_p = 0.1065, 0.1544, 0.3016$ and 0.3916, and four different l_c 's; (iii) 16 microstructures with $n = 4.27$, $v_p = 0.1043, 0.2474, 0.4832, 0.6273$ and four l_c 's; and (iv) a microstructure with $n \rightarrow \infty$. An example of the SG-RVE FE model containing spherical precipitates of 39.16% volume fraction and different channel widths, discretized into eight-noded brick elements, is depicted in Fig. 6a. In Fig. 6b, the homogenized AE-CP model parameters are calibrated with the averaged stress–strain responses from the RVE model.

Table 2

Calibrated constant material parameters for the grain scale AE-CP model.

Parameters	Q (J)	p	q	$\dot{\gamma}_0$ (s ⁻¹)	h_0 (MPa)	r
Value	6.5×10^{-19}	0.78	1.15	5.0×10^7	1300	1.115

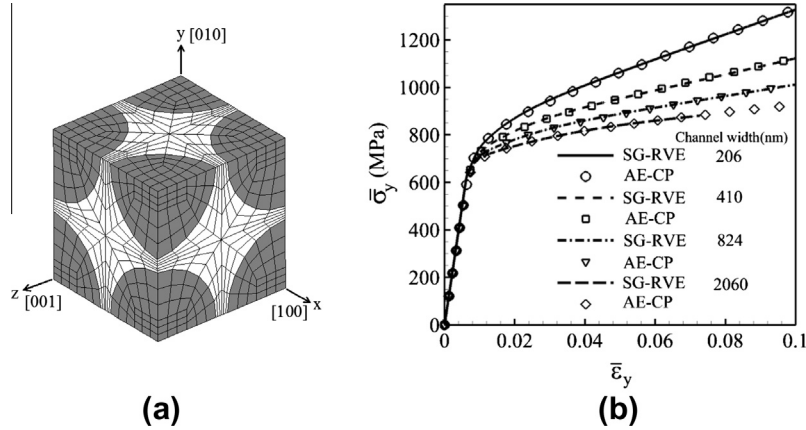


Fig. 6. Calibration of morphology-dependent homogenized crystal plasticity parameters in the grain-level activation energy-based crystal plasticity (AE-CP) model: (a) FEM model of the SG-RVE (SG-RVE) with spherical precipitates of volume fraction 39.16%, and (b) stress–strain response by the SG-RVE and AE-CP FE models.

4.4. Functional forms of homogenized constitutive parameters

Functional forms of the constitutive parameters $s_{*0}^z(n_1, v_p, l_c)$, $k_*(n_1, v_p, l_c)$, $k(n_1, v_p, l_c)$ and $s_{sat}^z(n_1, v_p, l_c)$ in Eq. (17) are needed to represent the effect of morphology on the single-crystal behavior. To derive these functional forms by computational homogenization, a large number of SG-RVE model simulations with varying volume fractions, channel widths and shapes are conducted. The homogenized initial thermal shear resistance s_{*0}^z for different channel widths and volume fractions are plotted for a shape factor $n = 4.27$ in Fig. 7.

These extensive set of simulations yield the following functional forms, where the coefficients are determined by solving a set of least square minimization problems.

$$(I) \quad s_{*0}^z(n_1, v_p, l_c) = a_1(n_1, v_p) + \frac{b_1(n_1, v_p)}{\sqrt{l_c}} \\ = 1039 + 559v_p - 99n_1 - 136v_p n_1 \\ + \frac{-0.1 + 89v_p + 53n_1 - 90v_p n_1}{\sqrt{l_c}} \quad (18)$$

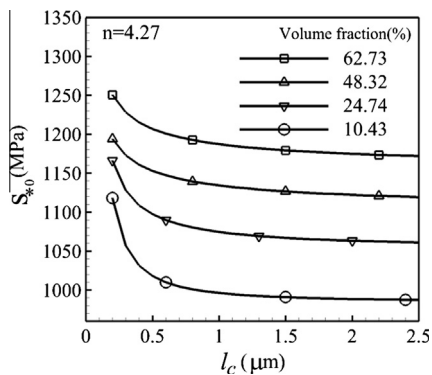


Fig. 7. Variation of the initial thermal shear resistance with different channel width and volume fractions of precipitates with $n = 4.27$.

$$(II) \quad s_{sat}^z(n_1, v_p, l_c) = a_2(n_1, v_p) + \frac{b_2(n_1, v_p)}{l_c} \\ = 3185 - 8905v_p - 1648n_1 + 6680v_p n_1 \\ + \frac{-0.21 + 5008v_p + 363n_1 - 3599v_p n_1}{l_c} \quad (19)$$

$$(III) \quad k_*(n_1, v_p, l_c) = 65 - 7500v_p + 33n_1 - 2700l_c \\ + 12768v_p n_1 - 23120v_p l_c \\ + 4080n_1 l_c - 19847v_p n_1 l_c \quad (20)$$

$$(IV) \quad k(n_1, v_p, l_c) = a_3(n_1, v_p) + \frac{b_3(n_1, v_p)}{\sqrt{l_c}} \\ = 5.5 - 327.6v_p + 31.5n_1 + 221.4v_p n_1 \\ + \frac{0.14 + 281.2v_p - 2.44n_1 - 176.5v_p n_1}{\sqrt{l_c}} \quad (21)$$

The explicit dependence on channel width l_c reflects the size effect due to the presence of GNDs in the subgrain dislocation density CP model. In Eqs. (18)–(21) the unit of l_c is μm , while the units of initial thermal resistance and saturation shear resistance in Eqs. (18) and (19) are MPa.

4.5. Validation of the homogenized AE-CP model

Two sets of validation tests are conducted for the homogenized AE-CP constitutive model. In the first set, the results of a single-grain crystal plasticity FEM analysis with the calibrated homogenized parameters are compared with the averaged response of an SG-RVE analysis. Three cases, corresponding to different microstructures, are considered for simulation. These are: Case 1: $n = 10$, $v_p = 44\%$, $l_c = 0.135 \mu\text{m}$; Case 2: $n = 1.5$, $v_p = 22\%$, $l_c = 0.260 \mu\text{m}$; and Case 3: $n = \infty$, $v_p = 30\%$, $l_c = 0.576 \mu\text{m}$. Simulations for both the AE-CP and SG-RVE FE models are conducted for an applied strain rate of 0.0001 s^{-1} in the y -direction at $800 \text{ }^\circ\text{C}$. The true stress–logarithmic strain

response by the AE-CP FE model and the averaged stress–strain response by the SG-RVE FE model are plotted in Fig. 8. Excellent agreement is obtained between the homogenized grain-scale model with morphological parameters and the explicit SG-RVE model. A notable advantage of the homogenized model is the significant efficiency gain over explicit RVE models. For this example, the gain in efficiency is of the order of 10^4 (a few seconds for AE-CP FE model over more than 100 h for SG-RVE FE model) with identical response. This efficiency advantage is necessary when modeling the polycrystalline microstructure of superalloys.

The second set involves validating the AE-CP constitutive model with results from creep experiments in Refs. [43,44] for single-crystal CMSX-4 with 70% volume fraction of γ' precipitates. In Ref. [43] a tensile load of 675 MPa is applied in the [1 1 1] direction at 800 °C, while in Ref. [44] the tensile load of 770 MPa is applied in the [001] direction at 750 °C. CPFEM analyses with the homogenized parameters are conducted for a single grain under these conditions. The simulated logarithmic strain–time response of the simulations agrees well with the experimental results in Fig. 9.

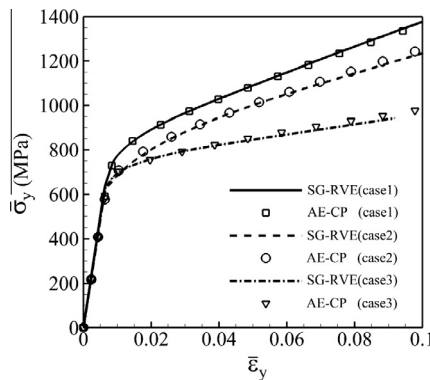


Fig. 8. Validation of the homogenized grain-level AE-CP model with a FEM model of the SG-RVE for three different microstructures.

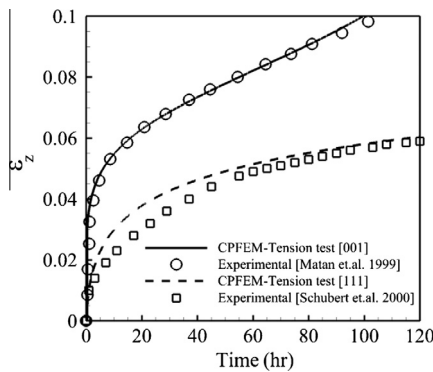


Fig. 9. Comparing the creep response by the homogenized AE-CP FEM with experiments in Refs. [43,44] for validating the grain-scale crystal plasticity model. Tension tests in [001] and [111] directions are for 770 MPa @ 750 °C and 675 MPa @ 800 °C respectively.

5. Microtwin nucleation and evolution in grain-scale CP model

Single-crystal experiments on Ni-based superalloys have shown considerable tension–compression asymmetry. A considerable difference in the creep response of single crystals loaded in the [001] and [011] directions under tension and compression conditions has been reported in Ref. [36,45]. APB shearing is responsible for the difference in tension and compression tests in the [001] direction. However, the TEM observations in Ref. [7] show a microtwinning mechanism for high-temperature creep deformation. To account for this tension–compression asymmetry observation, a microtwinning model, developed in Ref. [7], is incorporated into the grain-scale crystal plasticity model. The criterion for microtwin nucleation in Ref. [7] is based on the state of dissociation of the leading and trailing partials on a slip system, where the condition for dissociation of a full dislocation $a/2\langle 110 \rangle$ is given as a function of the magnitude and orientation of the in-plane shear stress. With deformation, the leading and trailing Shockley partials experience stresses τ_{lead} and τ_{trail} , respectively. From the magnitudes of the in-plane resolved shear stress $\tau^{inplane}$ and stresses τ_{lead} and τ_{trail} , the criterion examines whether the partials will remain together or dissociate at the interface of the γ – γ' phases. Thus, if $\|\tau^{inplane}\| > \tau_{lead}$, $\|\tau^{inplane}\| < -\tau_{trail}$, the leading partial passes through and hence the leading and trailing partials dissociate. The direction of dislocation is also another determinant for dissociation. This condition is applied to yield asymmetry due to the difference in the direction of dislocation motion for tension and compression.

The microtwin evolution model is based on the premise that γ' precipitate shearing and subsequent reordering is the predecessor to the movement of partials causing plastic slip. The thermal reordering rate by diffusion depends on the activation energy barrier, i.e. $R_{reorder} \propto \exp(-\frac{\Delta E + p\Delta V_{act} - \theta\Delta S}{k_B\theta})$, where ΔE is the internal energy barrier, p is the pressure, ΔV_{act} is the activation volume for pressure dependent diffusion, ΔS is the change in entropy, k_B is Boltzmann's constant and θ is the absolute temperature. For solids, the pressure dependent activation volume ΔV_{act} is small and is hence ignored. The change in entropy occurs due to irreversible dissipation such as plastic work and is expressed as: $\theta\Delta S = W_p = \tau_{eff}A_p b_{tp}$, where τ_{eff} is the effective shear stress, A_p is the shearing area during plastic deformation and b_{tp} is the Burgers vector of the twin partials. The velocity of twin partials may be written as:

$$v_{tp} = f_{reorder} \lambda_{reorder} P_{reorder} (\Delta E, \theta\Delta S) \quad (22)$$

where $f_{reorder}$ is the frequency of reordering, $\lambda_{reorder}$ is the reordering distance and $P_{reorder}$ is the probability of reordering against the energy barrier, which is a function of plastic dissipation and internal energy barrier. The internal energy barrier is expressed as $\Delta E = \Gamma(t)A_{eff}$, where $\Gamma(t)$ is the energy drop, which decreases exponentially with time

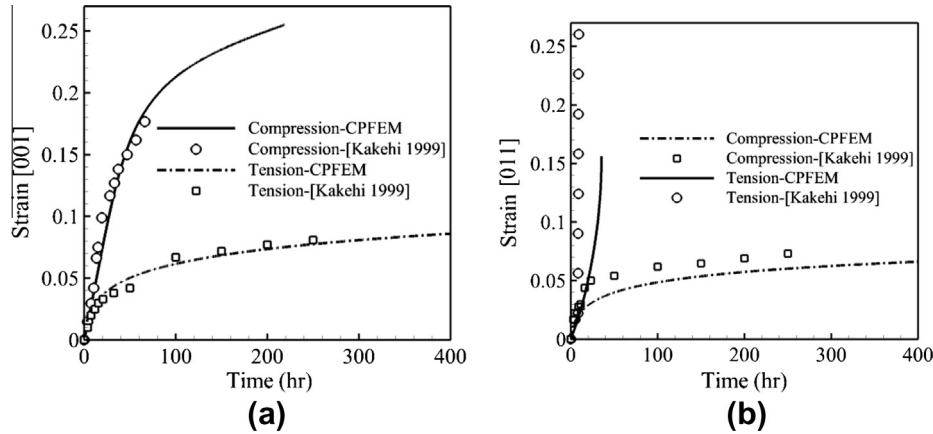


Fig. 10. Comparison of the logarithmic strain–time response of the homogenized AE-CP FE model, including microtwin nucleation and evolution, with experimental data [46] for tension and compression creep in (a) [001] and (b) [011] directions.

from pseudo-twin energy Γ_{pt} to true twin energy Γ_{tt} , where $\Gamma(t) = (\Gamma_{pt} - \Gamma_{tt}) \exp(-Kt) + \Gamma_{tt}$. The effective shear stress, including the effect of tertiary γ' precipitates, is expressed in Ref. [46] as $\tau_{eff} = \tau - \frac{f_3}{2} \frac{\Gamma_{pt}}{b_{ip}}$, where f_3 is the volume fraction of the tertiary γ' precipitates. The plastic shear strain rate due to microtwinning is then written from the Orowan equation as:

$$\dot{\gamma} = \rho_{ip} b_{ip} \lambda_{reorder} f_{reorder} \exp \left\{ -\frac{A_{eff} \Gamma(t) - V_{act} \tau_{eff}}{k_B \theta} \right\} \quad (23)$$

where ρ_{ip} is the density of partials which is a function of applied stress and time.

The homogenized AE-CP model, along with the grain-scale microtwin nucleation and evolution model in Eqs. (12)–(23), is employed to simulate the creep response of single-crystal superalloys. Significant tension–compression asymmetry is observed in the experimental data plotted in Fig. 10 for a single-crystal specimen [45]. Microtwin formation is not seen for tension loading in the [001] direction. However, a significant microtwin develops for compression in this direction, as observed in the TEM studies of Ref. [45]. Deformation is dominated by the strain due to the microtwin evolution, as shown in Fig. 10a. Similar observations are also made in experiments with loading in the [011] direction. For tensile and compressive creep tests, the observed trend, shown in Fig. 10b, is the opposite of that in the [001] direction. Microtwins in the deformed microstructure are observed for tension loading in the [011] direction, whereas no microtwin induced deformation is seen for compression loading. The results of the compression creep experiments with single crystals containing a 70% volume fraction of cubic precipitates in Refs. [36,46] are used to calibrate the material constants in Eq. (23). For compression tests, the loading conditions and microstructures are the same as in the tensile tests described in Section 4.3. The calibrated values of the material constants are: $\rho_{ip} = 1.0e11 \text{ m}^{-2}$, $b_{ip} = 0.145 \text{ }\mu\text{m}$, $\lambda_{reorder} = 0.3$, $f_{reorder} = 1.0$, $\Gamma_{pt} = 0.7 \text{ J m}^{-2}$ and $\Gamma_{tt} = 0.02 \text{ J m}^{-2}$. The results of the CPFEM simulation are compared with the

experimental data [45] in Fig. 10. The grain-scale CPFEM model satisfactorily predicts the single-crystal experimental data, including the microtwin induced tension–compression asymmetry.

6. Conclusions

This paper creates a hierarchical framework for realizing a homogenized grain-scale constitutive model that can be used for modeling polycrystalline microstructures of Ni-based superalloys. Specifically, an AE-CP FEM model is developed that incorporates characteristic parameters of the subgrain scale γ – γ' morphology. Hardening evolution laws are developed to reflect the effect of dislocation density distributions from the SG-RVE model, which represents deformation mechanisms in the temperature range $650 \text{ }^\circ\text{C} \leq \theta \leq 800 \text{ }^\circ\text{C}$. A significant advantage of this homogenized model is that its high efficiency enables it to be effectively incorporated in polycrystalline crystal plasticity FE simulations, while retaining the accuracy of detailed RVE models. The homogenized model incorporates the effect of important characteristics of the subgrain γ – γ' morphology, viz. the volume fraction and shape of the γ' precipitates and the γ channel width. Parametric representations of these subgrain morphology variables are incorporated in evolution laws of the homogenized AE-CP model that include both thermal and athermal shear resistance. The simplified RVEs with uniformly distributed generalized ellipsoidal particles provide a demonstrative platform for modeling framework connecting two scales, one with explicit representation and the other with their respective parametric forms. Three homogenized parameters, viz. the thermal shear resistance, the saturation shear resistance and the reference slip-rate $\dot{\gamma}_*$, are expressed as functions of the subgrain morphology variables. Size dependence, which is explicitly represented in the subgrain dislocation density crystal plasticity model through the presence of GNDs, is reflected in the homogenized AE-CP model through the explicit dependence on the channel

width. The homogenized AE-CP model is found to accurately reproduce the stress–strain response of the detailed γ – γ' RVE for a range of microstructural variations. It is also found to agree quite well with results of experimental studies on single-crystal superalloys in the literature. Finally, a microtwin nucleation and evolution model is incorporated alongside the homogenized AE-CP model for single crystals. Tension–compression asymmetry, observed in creep experiments in the literature, is represented very well by this model. The overall hierarchical model has the potential of significantly expediting polycrystalline crystal plasticity FE simulations while retaining accuracy. This is necessary for meaningful simulations that can be corroborated by experiments.

Acknowledgements

This work was partially supported by the National Science Foundation, Civil and Mechanical Systems Division through Grant No. CMMI-0800587 (program director: Dr. Clark Cooper), and by GE Aviation (program monitor: Dr. David Mourer). This sponsorship is gratefully acknowledged. The authors also acknowledge the discussions with Professors M.J. Mills and Y. Wang of the Ohio State University.

References

- [1] McLean M, Cahn RW. Nickel-base superalloys: current status and potential, high temperature structural materials. London: Chapman & Hall; 1996.
- [2] Sugui T, Jun X, Xiaoming Z, Benjiang Q, Jianwei L, Lili Y, et al. *Mater Sci Eng* 2011;A528:2076–84.
- [3] Epishin A, Link T, Brückner U, Portella PD. *Acta Mater* 2001;49:4017–23.
- [4] Pollock TM, Sammy T. *J Prop Power* 2006;22(2):361–75.
- [5] Ignat M, Buffiere JY, Chaix JM. *Acta Mater* 1993;41:855–62.
- [6] Viswanathan GB, Sarosi PM, Whitis DH, Mills MJ. *Mater Sci Eng* 2005;A400:489–95.
- [7] Unocic RR, Zhou N, Kovarik L, Shen C, Wang Y, Mills MJ. *Acta Mater* 2011;59:7325–39.
- [8] Chatterjee D, Hazari N, Das N, Mitra R. *Mater Sci Eng* 2010;A528:604–13.
- [9] Cormier J, Milhet X, Mendez J. *Acta Mater* 2007;55:6250–9.
- [10] Torster F, Baumeister G, Albrecht J, Lütjering G, Helm D, Daeubler MA. *Mater Sci Eng* 1997;A234–236:189–92.
- [11] Hong HU, Kim IS, Choi BG, Kim MY, Jo CY. *Mater Sci Eng* 2009;A517(1–2):125–31.
- [12] Pollock T, Argon A. *Acta Metall* 1992;40:1–30.
- [13] Nouailhas D, Cailletaud G. *Scripta Mater* 1996;34(4):565–71.
- [14] Ohashi T, Hidaga K, Saito M. *Mater Sci Eng* 1997;A238:42–9.
- [15] Busso E, Meissonier F, O'Dowd N. *J Mech Phys Sol* 2000;48:2333–61.
- [16] Busso E, Cheong K. *J Phys IV* 2001;11:161–70.
- [17] Dimiduk DM, Uchic MD, Parthasarathy TA. *Acta Mater* 2005;53:4065–77.
- [18] Choi YS, Parthasarathy T, Dimiduk D, Uchic M. *Mater Sci Eng A* 2005;397:69–83.
- [19] Probst H, Dlouhy A, Eggeler G. *Acta Mater* 1999;47:2497–510.
- [20] Manonukul A, Dunne FPE, Knowles D. *Acta Mater* 2002;50(11):2917–31.
- [21] Fedelich B. *Int J Plast* 2002;18:1–49.
- [22] Shenoy M, Kumar RS, McDowell D. *Int J Fatigue* 2005;27:1113–27.
- [23] Shenoy M, Zhang J, McDowell D. *Fatigue Fract Eng Mater Struct* 2007;30(10):889–904.
- [24] Shenoy M. PhD thesis, Georgia Institute of Technology; 2006.
- [25] Song JE. MS thesis, Georgia Institute of Technology; 2010.
- [26] Fromm BS, Chang K, McDowell DL, Chen L, Garmestani H. *Acta Mater* 2012;60:5984–99.
- [27] Feyel F, Chaboche J-L. *Comput Meth Appl Mech Eng* 2000;183:309–30.
- [28] Zohdi T, Oden JT, Rodin G. *Comput Meth Appl Mech Eng* 1999;172:3–25.
- [29] Ghosh S, Anahid M. Part 1. *Int J Plast* 2013;47:182–200.
- [30] Jain J, Ghosh S. *ASME J Appl Mech* 2008;75(3):031011-1–031011-15.
- [31] Ghosh S, Bai J, Paquet D. *J Mech Phys Sol* 2009;57:1017–44.
- [32] Ma A, Roters F. *Acta Mater* 2004;52:3603–12.
- [33] Ma A, Roters F, Raabe D. *Acta Mater* 2006;54:2169–79.
- [34] Arsenlis A, Parks D. *J Mech Phys Sol* 2002;50:1979–2009.
- [35] Fleury G, Schubert F, Nickel H. *Comput Mater Sci* 1996;7:187–93.
- [36] Knowles DM, Gunturi S. *Mater Sci Eng* 2002;A328:223–37.
- [37] Kayser FX, Stassis C. *Phys Status Solidi* 1981;64:335–42.
- [38] Kocks UF, Argon AS, Ashby AF. Thermodynamics and kinetics of slip. In: *Progress in materials science*, vol. 19. Oxford: Pergamon Press; 1975. p. 1–289.
- [39] Frost HJ, Ashby MF. Deformation-mechanism-map. In: *The plasticity and creep of metals and ceramics*. Oxford: Pergamon Press; 1982.
- [40] Xie CL, Ghosh S, Groeber M. *J Eng Mater Tech* 2004;126:339–52.
- [41] Kothari M, Anand L. *J Mech Phys Sol* 1998;46:51–83.
- [42] Hill R. *Math Proc Cam Phil Soc* 1984;95:481–94.
- [43] Schubert F, Fleury G, Steinhaus T. *Mod Simul Mater Sci Eng* 2000;8:947–57.
- [44] Matan N, Cox DC, Carter P, Rist MA, Rae CMF, Reed RC. *Acta Mater* 1999;47:1549–63.
- [45] Takehi K. *Scripta Mater* 1999;41(5):461–5.
- [46] Karthikeyan S, Unocic RR, Sarosi PM, Viswanathan GB, Whitis DD, Mills MJ. *Scripta Mater* 2006;54:1157–62.